Comparing DG and Nédélec Finite Element Discretisations of the Second-Order Time-Domain Maxwell Equation

D. Sármány[a,*], M.A. Botchev[a], J.J.W. van der Vegt[a], J.G. Verwer[b]

[a] *Department of Applied Mathematics, University of Twente, P.O. Box 217, 7500 AE Enschede, the Netherlands*
[b] *Center for Mathematics and Computer Science, P.O. Box 94079, 1090 GB Amsterdam, the Netherlands*

Abstract

This article compares the discontinuous Galerkin finite element method (DG-FEM) with the $H(\mathrm{curl})$-conforming FEM in the discretisation of the second-order time-domain Maxwell equations with possibly nonzero conductivity term. While DG-FEM suffers from an increased number of degrees of freedom compared with $H(\mathrm{curl})$-conforming FEM, it has the advantage of a purely block-diagonal mass matrix. This means that, as long as an explicit time-integration scheme is used, it is no longer necessary to solve a linear system at each time step – a clear advantage over $H(\mathrm{curl})$-conforming FEM. It is known that DG-FEM generally favours high-order methods whereas $H(\mathrm{curl})$-conforming FEM is more suitable for low-order ones. The novelty we provide in this work is a direct comparison of the performance of the two methods when hierarchic $H(\mathrm{curl})$-conforming basis functions are used up to polynomial order $p = 3$. The motivation behind this choice of basis functions is its growing importance in the development of p- and hp-adaptive FEMs.

The fact that we allow for nonzero conductivity requires special attention with regards to the time-integration methods applied to the semi-discrete systems. High-order polynomial basis warrants the use of high-order time-integration schemes, but existing high-order schemes may suffer from a too severe time-step stability restriction as result of the conductivity term. We investigate several alternatives from the point of view of accuracy, stability and computational work. Finally, we carry out a numerical Fourier analysis to study the dispersion and dissipation properties of the semi-discrete DG-FEM scheme and several of the time-integration methods. It is instructive in our approach that the dispersion and dissipation properties of the spatial discretisation and those of the time-integration methods are investigated separately, providing additional insight into the two discretisation steps.

Keywords: $H(\mathrm{curl})$-conforming finite element method, discontinuous Galerkin finite element method, numerical time integration, second-order Maxwell wave equation

1. Introduction

High-order finite element methods (FEM) are an increasingly important technology in large-scale electromagnetic simulations thanks to their ability to effectively model complex geometrical structures and long-time wave propagation. It has long been known that the standard H^1-conforming FEM for electromagnetic waves may result in non-physical, spurious solutions. Instead, one may naturally opt for the $H(\mathrm{curl})$-conforming FEM pioneered by Nédélec [1, 2] and Bossavit [3, 4]. It has the advantage of mimicking the geometrical properties of the Maxwell equations at the discrete level. However, in time-domain computations it requires solving linear systems with mass matrices even if an explicit time-integration method is used. One attractive alternative – also free of spurious solutions under certain conditions – is the discontinuous Galerkin FEM (DG-FEM) [5, 6, 7], where the resulting mass matrix is block-diagonal and therefore the computational cost of its inversion is negligible. But this additional flexibility comes at a cost. The number of degrees of freedom in DG discretisations is higher than that in the $H(\mathrm{curl})$-conforming discretisation, although the difference decreases as the polynomial order in the

*Corresponding author
Email addresses: d.sarmany@math.utwente.nl (D. Sármány), m.a.botchev@math.utwente.nl (M.A. Botchev), j.j.w.vandervegt@math.utwente.nl (J.J.W. van der Vegt), jan.verwer@cwi.nl (J.G. Verwer)

spatial discretisation grows. As an illustration, Figure 1 shows the sparsity patterns of the mass matrices for both methods when a mesh of 320 tetrahedra and third-order polynomials are used.

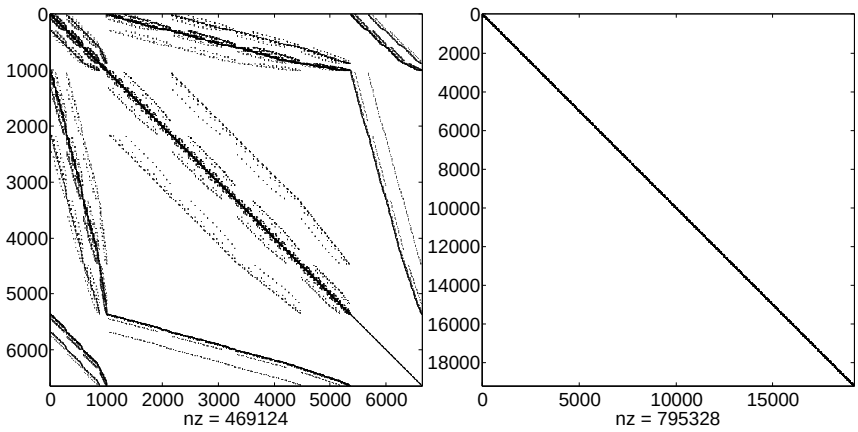

Figure 1: Sparsity pattern of the mass matrix for $H(\mathrm{curl})$-conforming FEM (left) and DG-FEM (right) for a mesh with 320 elements. Third-order polynomials are used, which means that the size of the blocks in the right plot is 60×60. Note the difference in size between the two matrices.

So there appears to be a trade-off between the two methods in time-domain computations. In general, the $H(\mathrm{curl})$-conforming approach is more efficient with low-order polynomials and DG-FEM with high-order ones. The expected break-even point depends on a number of factors, such as the conditioning and sparsity of the mass and stiffness matrices in the resulting semi-discrete systems. As a novelty, the focus of this work is to provide a comparison of the computational performance of the two methods when hierarchic $H(\mathrm{curl})$-conforming basis functions [8, 9] are used on tetrahedral meshes. The motivation behind this choice is that these basis functions play an ever more important role in the development of p- and hp-adaptive methods [10] for the Maxwell equation.

Throughout the article, the different discretisation techniques are applied to the three-dimensional Maxwell equations in the second-order time-dependent form,

$$\varepsilon_{\mathrm{r}}\frac{\partial^2 \boldsymbol{E}}{\partial t^2} + \sigma\frac{\partial \boldsymbol{E}}{\partial t} + \nabla\times\left(\mu_{\mathrm{r}}^{-1}\nabla\times\boldsymbol{E}\right) = -\frac{\partial \boldsymbol{J}}{\partial t}, \tag{1}$$

with homogeneous boundary conditions $\boldsymbol{n}\times\boldsymbol{E}=\boldsymbol{0}$. All quantities are dimensionless[1] in (1), where $\boldsymbol{E}$ is the electric field and $\boldsymbol{J}$ is the electric current density. The values σ, ε_{r} and μ_{r} are assumed to be time-independent constant scalars, and they respectively denote conductivity, relative dielectric permittivity and relative magnetic permeability. If the domain is filled with nonconductive material, the damping term $\sigma\frac{\partial \boldsymbol{E}}{\partial t}$ is absent. If, in addition, the source term $-\partial_t\boldsymbol{J}$ is also taken to be zero, we have the conservative Maxwell wave equation.

Following the method of lines, we first discretise the spatial operators, using the $H(\mathrm{curl})$-conforming FEM or the DG-FEM. In either case, we arrive at a semi-discrete system in the form of second-order ordinary differential equations (ODEs) in $\mathbb{R}^n$,

$$M_\varepsilon u'' + M_\sigma u' + S_\mu u = j, \tag{2}$$

where u is the unknown vector of N scalar coefficients associated with the approximation of the electric field $\boldsymbol{E}$. The source term j is the projection of $-\partial_t\boldsymbol{J}$ onto the finite-element space and in general may also contain boundary data. For simplicity, however, we restrict ourselves to the homogeneous Dirichlet

[1] We can derive the dimensionless form by using the scalings $\boldsymbol{x}=\tilde{\boldsymbol{x}}/\tilde{L}$, $t=\tilde{t}/(\tilde{L}/\tilde{c}_0)$, $\boldsymbol{E}=\tilde{\boldsymbol{E}}/(\tilde{Z}_0\tilde{H}_0)$, $\boldsymbol{H}=\tilde{\boldsymbol{H}}/\tilde{H}_0$, $\boldsymbol{J}=\tilde{\boldsymbol{J}}/(\tilde{H}_0/\tilde{L})$ and $\sigma=\tilde{\boldsymbol{J}}\tilde{L}\tilde{Z}_0/\tilde{\boldsymbol{E}}$, with tilde denoting the dimensional quantities. Here $\tilde{L}$ is the reference length, $\tilde{c}_0=(\tilde{\mu}_0\tilde{\varepsilon}_0)^{-1/2}$ is the speed of light in vacuum, $\boldsymbol{H}$ is the magnetic field (eliminated in (1)), $\tilde{H}_0$ is the reference magnetic field strength and $\tilde{Z}_0=(\mathrm{i}\tilde{\omega}\tilde{\mu}_0/(\tilde{\sigma}+\mathrm{i}\tilde{\omega}\tilde{\varepsilon}_0))^{1/2}$ is the intrinsic impedance, with $\tilde{\omega}$ being the angular frequency and i the imaginary unit.

boundary condition, $\boldsymbol{n} \times \boldsymbol{E} = \boldsymbol{0}$, in this article. Each term in the left-hand side of (2) corresponds to the respective term in the left-hand side of (1). The mass matrix M_ε is symmetric positive definite and the conductivity matrix M_σ is symmetric positive semi-definite. In addition, for constant scalars σ and ε_r the matrices M_ε and M_σ are identical up to a constant. The stiffness matrix S_μ is the discretisation of the wave term and is symmetric positive semi-definite.

Convergence results for the $H(\mathrm{curl})$-conforming semi-discrete approximation (2) are relatively well-established [11, 12]. Results on the semi-discrete DG discretisation are more recent: energy-norm estimates [13] and L^2-estimates [14] have been derived for the Maxwell equations; optimal error estimates for the fully-discrete second-order scalar wave equation have been provided in [15]; and a promising energy-conserving local-time stepping scheme has been developed in [16].

A vital feature of (1) and (2) from the point of view of time integration is that it includes the conductivity σ. Even moderate values of σ may result in a prohibitively small time step for many of the popular time-integration schemes. Therefore, we pay special attention to time-integration methods that treat the conductivity mass matrix M_σ in an implicit way. Many of such methods and others discussed in this article have been previously studied in [17] for the system of first-order Maxwell equations discretised by the lowest-order $H(\mathrm{curl})$-conforming elements. See also [18] for more details on composition methods for the conduction-free Maxwell equations.

The semi-discrete system (2) conserves (discrete) energy for the spatial discretisations discussed here, since these are both symmetric. Hence, using an energy-conservative time-integration method results in a conservative fully-discrete scheme. We investigate the dispersion and dissipation error of the schemes in two steps. First, we determine the dispersion error of the semi-discrete scheme by solving the time-harmonic eigenvalue problem corresponding to the semi-discrete system. Second, we can then apply any given time-integration scheme to a simple, but equivalent, model problem that includes the information of the semi-discrete numerical frequency, and thus define the dispersion (and, if there is any, dissipation) error of the time-integration method. This approach shows if the dispersion error is dominated by the spatial or temporal discretisation – a piece of information that may prove useful in deciding whether or not to go for high-order time-integration schemes.

The computational performance of the $H(\mathrm{curl})$-conforming method hinges to a great degree on efficiently solving the linear system with the mass matrix. A number of advanced techniques have been proposed recently, including mass lumping [19, 20, 21], the explicit computation of an approximate sparse inverse mass matrix [22], or the construction of special preconditioners. These approaches, however, do not in their current states provide a general framework and therefore cannot be extended to high-order discretisations in a straightforward manner. That is the reason why in this article we resort to standard preconditioners. It is of course also possible to use sparse direct solvers but in test problems we found that they are too memory demanding for large-scale three-dimensional computations.

The remaining part of the article is organised as follows. The weak formulations of the $H(\mathrm{curl})$-conforming FEM and the DG-FEM are given in Section 2. The semi-discrete system arising from either of the spatial discretisations is analysed in Section 3, while we briefly describe a number of the most widely-used time-integration methods in Section 4. Numerical examples that compare the computational performance of the two finite element approaches are presented in Section 5, where we test both low-order and high-order approximations. Section 6 concludes the article with final remarks.

2. The weak formulation

Before we present the weak formulations that result from the $H(\mathrm{curl})$-conforming and the DG discretisations, we introduce the tessellation $\mathcal{T}_h$ that partitions the polyhedral domain $\Omega \subset \mathbb{R}^3$ into a set of tetrahedra $\{K\}$. Throughout the article we assume that the mesh is shape-regular and that each tetrahedron is straight-sided. The notations $\mathcal{F}_h$, $\mathcal{F}_h^i$ and $\mathcal{F}_h^b$ stand respectively for the set of all faces $\{F\}$, the set of all internal faces, and the set of all boundary faces.

On the computational domain Ω, we define the spaces

$$H(\mathrm{curl};\Omega) := \left\{ \boldsymbol{u} \in \left[L^2(\Omega)\right]^3 : \nabla \times \boldsymbol{u} \in \left[L^2(\Omega)\right]^3 \right\},$$

$$H_0(\mathrm{curl};\Omega) := \left\{ \boldsymbol{u} \in H(\mathrm{curl};\Omega) \;\middle|\; \boldsymbol{n} \times \boldsymbol{u} = \boldsymbol{0} \text{ on } \partial\Omega \right\},$$

and the L^2 inner product $(\cdot,\cdot)$

$$(\boldsymbol{u},\boldsymbol{v}) = \int_\Omega \boldsymbol{u}\cdot\boldsymbol{v}\,\mathrm{d}V.$$

The continuous weak formulation of (1) now reads as follows: Find $\boldsymbol{E} \in H_0(\mathrm{curl},\Omega)$ such that $\forall \boldsymbol{w} \in H_0(\mathrm{curl},\Omega)$ the relation

$$\frac{\partial^2}{\partial t^2}\left(\varepsilon_\mathrm{r}\boldsymbol{E},\boldsymbol{w}\right) + \frac{\partial}{\partial t}\left(\sigma\boldsymbol{E},\boldsymbol{w}\right) + \left(\mu_\mathrm{r}^{-1}\nabla\times\boldsymbol{E},\nabla\times\boldsymbol{w}\right) = -\left(\frac{\partial\boldsymbol{J}}{\partial t},\boldsymbol{w}\right) \tag{3}$$

is satisfied. See e.g. [23, 12].

2.1. Weak formulation of the globally H(curl)-conforming discretisation

In order to discretise (3), we first introduce the finite element space associated with the tessellation $\mathcal{T}_h$. Let $\mathcal{P}_p(K)$ be the space of polynomials of degree at most $p \geq 1$ on $K \in \mathcal{T}_h$. Over each element K the H(curl)-conforming polynomial space is defined as

$$Q^p = \left\{\boldsymbol{u} \in \left[\mathcal{P}_p(K)\right]^3;\ \boldsymbol{u}_T|_{F_i^K} \in \left[\mathcal{P}_p(F_i^K)\right]^2;\ \boldsymbol{u}\cdot\boldsymbol{\tau}_j|_{e_j^K} \in \mathcal{P}_p(e_j^K)\right\}, \tag{4}$$

where F_i^K, $i = 1,2,3,4$ are the faces of the element; e_j^K, $j = 1,2,3,4,5,6$ are the edges of the element; $\boldsymbol{u}_T$ is the tangential component of $\boldsymbol{u}$; and $\boldsymbol{\tau}_j$ is the directed tangential vector on edge e_j^K. For the construction of Q^p, we use a set of H(curl)-conforming hierarchic basis functions [8, 9].

Next, we introduce the discrete space of globally H(curl)-conforming functions

$$\Upsilon_h^p := \left\{\boldsymbol{v} \in \left[H_0(\mathrm{curl},\Omega)\right]^3 \;\middle|\; \boldsymbol{v}|_K \in Q^p,\ \forall K \in \mathcal{T}_h\right\},$$

and let the set of basis functions $\{\boldsymbol{\psi}_i\}$ span the space Υ_h^p. See [12] for a detailed discussion on both continuous and discrete H(curl)-conforming spaces. We can then approximate the electric field $\boldsymbol{E}$ as

$$\boldsymbol{E} \approx \boldsymbol{E}_h = \sum_i u_i(t)\boldsymbol{\psi}_i(x), \tag{5}$$

from which the discrete weak formulation reads as follows: Find $\boldsymbol{E}_h \in \Upsilon_h^p$ such that $\forall\boldsymbol{\phi} \in \Upsilon_h^p$ the relation

$$\frac{\partial^2}{\partial t^2}\left(\varepsilon_\mathrm{r}\boldsymbol{E}_h,\boldsymbol{\phi}\right) + \frac{\partial}{\partial t}\left(\sigma\boldsymbol{E}_h,\boldsymbol{\phi}\right) + \left(\mu_\mathrm{r}^{-1}\nabla\times\boldsymbol{E}_h,\nabla\times\boldsymbol{\phi}\right) = -\left(\frac{\partial\boldsymbol{J}}{\partial t},\boldsymbol{\phi}\right) \tag{6}$$

is satisfied. Note that (6) is satisfied if and only if it is satisfied for every basis function $\boldsymbol{\psi}_i, i = 1,\ldots,N$, with N being the global number of degrees of freedom. As a result, substitution of (5) into (6) yields the semi-discrete system (2) with

$$\begin{aligned}
[M_\varepsilon]_{ij} &= \left(\varepsilon_\mathrm{r}\boldsymbol{\psi}_i,\boldsymbol{\psi}_j\right), \quad [S_\mu]_{ij} = \left(\mu_\mathrm{r}^{-1}\nabla\times\boldsymbol{\psi}_i,\nabla\times\boldsymbol{\psi}_j\right),\\
[M_\sigma]_{ij} &= \left(\sigma\boldsymbol{\psi}_i,\boldsymbol{\psi}_j\right), \quad [j]_i = -\left(\frac{\partial\boldsymbol{J}}{\partial t},\boldsymbol{\psi}_i\right).
\end{aligned}$$

Each of the above matrices – M_ε, M_σ and S_μ – has a large number entries far off the diagonal, increasing the computational cost for both explicit and implicit time-integration methods.

2.2. Weak formulation of DG-FEM

In contrast to the H(curl)-conforming discretisation, in DG-FEM we are looking for the discrete solution in the space

$$\Sigma_h^p := \left\{\boldsymbol{\sigma} \in \left[L^2(\Omega)\right]^3 \;\middle|\; \boldsymbol{\sigma}|_K \in Q^p,\ \forall K \in \mathcal{T}_h\right\}.$$

That is, we allow the polynomial functions to be fully discontinuous across element interfaces and assume that the set of basis functions $\{\boldsymbol{\psi}_i\}$ now span the space Σ_h^p. Instead of enforcing continuity of the tangential components, the information between elements is now coupled through the numerical flux

[5, 24, 7]. Before we can define the numerical flux and formulate the discretisation for DG-FEM, we first need to introduce more notation.

Consider an interface $F \in \mathcal{F}_h$ between element K^L and element K^R, and let $\boldsymbol{n}^L$ and $\boldsymbol{n}^R$ represent their respective outward pointing normal vectors. We define the tangential jump and the average of the quantity $\boldsymbol{u}$ across interface F as

$$[\![\boldsymbol{u}]\!]_T = \boldsymbol{n}^L \times \boldsymbol{u}^L + \boldsymbol{n}^R \times \boldsymbol{u}^R \quad \text{and} \quad \{\!\{\boldsymbol{u}\}\!\} = \left(\boldsymbol{u}^L + \boldsymbol{u}^R\right)/2,$$

respectively. Here $\boldsymbol{u}^L$ and $\boldsymbol{u}^R$ are the values of the trace of $\boldsymbol{u}$ at ∂K^L and ∂K^R, respectively. At the boundary Γ, we set $\{\!\{\boldsymbol{u}\}\!\} = \boldsymbol{u}$ and $[\![\boldsymbol{u}]\!]_T = \boldsymbol{n} \times \boldsymbol{u}$. We furthermore introduce the global lifting operator $\mathcal{R}(\boldsymbol{u}) : \left[L^2(\mathcal{F}_h)\right]^3 \to \Sigma_h^p$ as

$$(\mathcal{R}(\boldsymbol{u}), \boldsymbol{v})_\Omega = \int_{\mathcal{F}_h} \boldsymbol{u} \cdot \{\!\{\boldsymbol{v}\}\!\} \,\mathrm{d}A, \quad \forall \boldsymbol{v} \in \Sigma_h^p, \tag{7}$$

and, for a given face $F \in \mathcal{F}_h$, the local lifting operator $\mathcal{R}_F(\boldsymbol{u}) : \left[L^2(F)\right]^3 \to \Sigma_h^p$ as

$$(\mathcal{R}_F(\boldsymbol{u}), \boldsymbol{v})_\Omega = \int_{F} \boldsymbol{u} \cdot \{\!\{\boldsymbol{v}\}\!\} \,\mathrm{d}A, \quad \forall \boldsymbol{v} \in \Sigma_h^p. \tag{8}$$

Note that $\mathcal{R}_F(\boldsymbol{u})$ vanishes outside the elements connected to the face F so that for a given element $K \in \mathcal{T}_h$ we have the relation

$$\mathcal{R}(\boldsymbol{u}) = \sum_{F \in \mathcal{F}_h} \mathcal{R}_F(\boldsymbol{u}), \quad \forall \boldsymbol{u} \in \left[L^2(\mathcal{F}_h)\right]^3. \tag{9}$$

The discrete weak formulation for DG-FEM now reads as follows [25]: Find $\boldsymbol{E}_h \in \Sigma_h^p$ such that $\forall \boldsymbol{\phi} \in \Sigma_h^p$ the relation

$$\begin{aligned}\frac{\partial^2}{\partial t^2}\left(\varepsilon_\mathrm{r}\boldsymbol{E}_h, \boldsymbol{\phi}\right) + \frac{\partial}{\partial t}\left(\sigma\boldsymbol{E}_h, \boldsymbol{\phi}\right) + \left(\mu_\mathrm{r}^{-1}\nabla_h \times \boldsymbol{E}_h, \nabla_h \times \boldsymbol{\phi}\right) \\ - \int_{\mathcal{F}_h} [\![\boldsymbol{E}_h]\!]_T \cdot \{\!\{\nabla_h \times \boldsymbol{\phi}\}\!\} \,\mathrm{d}A - \int_{\mathcal{F}_h} \{\!\{\nabla_h \times \boldsymbol{E}_h\}\!\} \cdot [\![\boldsymbol{\phi}]\!]_T \,\mathrm{d}A \\ + \sum_{F \in \mathcal{F}_h} C_F \left(\mathcal{R}_F([\![\boldsymbol{E}]\!]_T), \mathcal{R}_F([\![\boldsymbol{\phi}]\!]_T)\right)_\Omega = -\left(\frac{\partial \boldsymbol{J}}{\partial t}, \boldsymbol{\phi}\right)\end{aligned} \tag{10}$$

is satisfied, where the operator ∇_h denotes the elementwise application of ∇. For stability, the constant C_F has to satisfy the condition [25]

$$C_F \geq n_f C_1 + \min\left\{\frac{1}{2}, \frac{1}{C_2}\right\},$$

where C_1 and C_2 are positive constants and n_f denotes the number of sides of each element, that is for tetrahedra $n_f = 4$. As a consequence, the constant C_F is independent of both the polynomial order and the mesh size.

Again, (10) is satisfied if and only if it is satisfied for every basis function $\boldsymbol{\psi}_i, i = 1, \ldots, N$, with N being the global number of degrees of freedom. Substitution of $\boldsymbol{E} \approx \boldsymbol{E}_h = \sum_i u_i(t)\boldsymbol{\psi}_i(x)$ into (10) yields the semi-discrete system (2) with

$$\begin{aligned}[M_\varepsilon]_{ij} &= \left(\varepsilon_\mathrm{r}\boldsymbol{\psi}_i, \boldsymbol{\psi}_j\right), \quad [M_\sigma]_{ij} = \left(\sigma\boldsymbol{\psi}_i, \boldsymbol{\psi}_j\right), \quad [j]_i = -\left(\frac{\partial \boldsymbol{J}}{\partial t}, \boldsymbol{\psi}_i\right), \\ [S_\mu]_{ij} &= \left(\mu_\mathrm{r}^{-1}\nabla_h \times \boldsymbol{\psi}_i, \nabla_h \times \boldsymbol{\psi}_j\right) - \int_{\mathcal{F}_h} [\![\boldsymbol{\psi}_i]\!]_T \cdot \left\{\!\!\left\{\nabla_h \times \boldsymbol{\psi}_j\right\}\!\!\right\} \mathrm{d}A \\ &\quad - \int_{\mathcal{F}_h} \left\{\!\!\left\{\nabla_h \times \boldsymbol{\psi}_i\right\}\!\!\right\} \cdot \left[\!\!\left[\boldsymbol{\psi}_j\right]\!\!\right]_T \mathrm{d}A + \sum_{F \in \mathcal{F}_h} C_F \left(\mathcal{R}_F([\![\boldsymbol{\psi}_i]\!]_T), \mathcal{R}_F(\left[\!\left[\boldsymbol{\psi}_j\right]\!\right]_T)\right)_\Omega.\end{aligned}$$

The matrices M_ε and M_σ are now block-diagonal with the elementwise matrices being the blocks. However, the stiffness matrix S_μ has still many entries far off the diagonal because of the face integrals in its construction. That is why, DG in general warrants the use of explicit time-integration schemes but not implicit ones.

We emphasise that (10) is only one of many possible formulations of DG-FEM, depending on the numerical flux one chooses to use. The one we have introduced here is based on the numerical flux from [26] (see also [27]), and was analysed in detail for the time-harmonic Maxwell equations in [25]. See also [24] for an overview of DG-FEM methods for elliptic problems and for a large number of possible choices for the numerical flux.

2.3. The energy norm

Convergence results for FEMs are generally derived not only in the L^2-norm but also in a norm associated with the discrete energy of the approximation [13, 15]. These are defined for the $H(\mathrm{curl})$-conforming and DG discretisations as

$$\|\boldsymbol{v}\|^2_{H(\mathrm{curl})} = \|\boldsymbol{v}\|^2 + \|\nabla \times \boldsymbol{v}\|^2$$

and

$$\|\boldsymbol{v}\|^2_{\mathrm{DG}} = \|\boldsymbol{v}\|^2 + \|\nabla_h \times \boldsymbol{v}\|^2 + \|\mathtt{h}^{-\frac{1}{2}} [\![\boldsymbol{v}]\!]_T \|^2_{\mathcal{F}_h},$$

respectively. In the above definition, $\|\cdot\|_{\mathcal{F}_h}$ denotes the $L^2(\mathcal{F})$ norm and $\mathtt{h}(\boldsymbol{x}) = h_F$ is the diameter of face F containing $\boldsymbol{x}$. We note that the two definitions of the energy norm are actually identical as ∇_h becomes ∇ and $[\![\cdot]\!]_T$ vanishes if $H(\mathrm{curl})$-conforming discretisation is used.

3. Stability of the semi-discrete system

To carry out a basic stability analysis, we first transform (2) into a first-order system of ODEs,

$$\begin{aligned} u' &= v, \\ M_\varepsilon v' + M_\sigma v + S_\mu u &= j. \end{aligned} \tag{11}$$

Recall that S_μ is symmetric and therefore – using the inner-product notation for discrete vectors – we have the property

$$\begin{aligned} \frac{\mathrm{d}}{\mathrm{d}t}\left(v^T M_\varepsilon v + u^T S_\mu u\right) = \frac{\mathrm{d}v^T}{\mathrm{d}t} M_\varepsilon v + v^T M_\varepsilon \frac{\mathrm{d}v}{\mathrm{d}t} + \frac{\mathrm{d}u^T}{\mathrm{d}t} S_\mu u + u^T S_\mu \frac{\mathrm{d}u}{\mathrm{d}t} = \\ 2v^T\left(-M_\sigma v - S_\mu u + j\right) + 2v^T S_\mu u = 2v^T j - 2v^T M_\sigma v. \end{aligned} \tag{12}$$

If $j = 0$, this entails stability, that is

$$\frac{\mathrm{d}}{\mathrm{d}t}\left(v^T M_\varepsilon v + u^T S_\mu u\right) = -2v^T M_\sigma v \le 0,$$

since, for constant σ, the matrix M_σ is positive definite if $\sigma > 0$ and $M_\sigma = 0$ if $\sigma = 0$. Therefore, if $\sigma = 0$ in addition to $j = 0$, (12) shows conservation.

In order to use a stability test model introduced later in this section, we transform (11) to an equivalent explicit form. To do so, we multiply the first equation in (11) with M_ε and introduce the Cholesky factorisation $LL^T = M_\varepsilon$. The new variables $\tilde{v} = L^T v$ and $\tilde{u} = L^T u$ then satisfy the system

$$\begin{pmatrix} \tilde{u}' \\ \tilde{v}' \end{pmatrix} = \begin{pmatrix} 0 & I \\ -\tilde{S}_\mu & -\tilde{M}_\sigma \end{pmatrix} \begin{pmatrix} \tilde{u} \\ \tilde{v} \end{pmatrix} + \begin{pmatrix} 0 \\ \tilde{j} \end{pmatrix}, \tag{13}$$

where

$$\tilde{j} = L^{-1} j, \quad \tilde{S}_\mu = L^{-1} S_\mu L^{-T}, \quad \tilde{M}_\sigma = L^{-1} M_\sigma L^{-T}.$$

Since both the conductivity coefficient σ and the permittivity coefficient ε_{r} are constant scalars in (1), the matrix $\tilde{M}_\sigma$ in (13) is the constant diagonal matrix

$$\tilde{M}_\sigma = \gamma I, \quad \gamma = \frac{\sigma}{\varepsilon_{\mathrm{r}}}.$$

From this we can derive a two-by-two system through which stability of time-integration methods for (11) can be examined.

The matrix $\tilde{S}_\mu$ is symmetric positive semi-definite so it can be decomposed as $\tilde{S}_\mu = U\Lambda U^T$, where Λ is a diagonal matrix with the eigenvalues of $\tilde{S}_\mu$ on its diagonal

$$\lambda_1 \geq \lambda_2 \geq \ldots \geq \lambda_r \geq \lambda_{r+1} = \lambda_{r+1} = \ldots = \lambda_n = 0,$$

where r is the rank of the matrix. The matrix U is orthogonal and its columns are the eigenvectors of $\tilde{S}_\mu$. Using a permutation matrix $\mathcal{P}$, we have

$$\mathcal{A} = \begin{pmatrix} 0 & I \\ -\tilde{S}_\mu & -\tilde{M}_\sigma \end{pmatrix} = \begin{pmatrix} 0 & UU^T \\ -U\Lambda U^T & -\gamma I \end{pmatrix} = \\ \begin{pmatrix} U & 0 \\ 0 & U \end{pmatrix} \begin{pmatrix} 0 & I \\ -\Lambda & -\gamma I \end{pmatrix} \begin{pmatrix} U^T & 0 \\ 0 & U^T \end{pmatrix} = \begin{pmatrix} U & 0 \\ 0 & U \end{pmatrix} \mathcal{P}\Lambda_{\mathcal{P}}\mathcal{P}^T \begin{pmatrix} U^T & 0 \\ 0 & U^T \end{pmatrix}, \quad (14)$$

where $\Lambda_{\mathcal{P}}$ is a block-diagonal matrix with two-by-two blocks

$$\begin{pmatrix} 0 & 1 \\ -\lambda_k & -\gamma \end{pmatrix}, \qquad k = 1, \ldots, N. \quad (15)$$

This allows us to state the following proposition.

Proposition 1. *Assume that σ and ε_{r} are scalar and $\gamma = \sigma/\varepsilon_{\mathrm{r}}$. Then the matrix $\mathcal{A}$ has*

(i) $n - r$ *zero eigenvalues,*

(ii) $n - r$ *eigenvalues which equal* $-\gamma$*,*

(iii) $2r$ *eigenvalues which are*

$$\frac{-\gamma \pm \sqrt{\gamma^2 - 4\lambda_k}}{2}, \quad k = 1, \ldots, r.$$

Thus, the orthogonal transformation $V \equiv \left(\begin{smallmatrix} U & 0 \\ 0 & U \end{smallmatrix}\right)\mathcal{P}$ decouples (13) into r two-by-two systems

$$\begin{pmatrix} \hat{u}' \\ \hat{v}' \end{pmatrix} = \begin{pmatrix} 0 & 1 \\ -\lambda & -\gamma \end{pmatrix} \begin{pmatrix} \hat{u} \\ \hat{v} \end{pmatrix} + \begin{pmatrix} 0 \\ \hat{j} \end{pmatrix},$$

with $\lambda = \lambda_k > 0$, $k = 1, \ldots, r$, and $n - r$ two-by-two systems

$$\begin{pmatrix} \hat{u}' \\ \hat{v}' \end{pmatrix} = \begin{pmatrix} 0 & 1 \\ 0 & -\gamma \end{pmatrix} \begin{pmatrix} \hat{u} \\ \hat{v} \end{pmatrix} + \begin{pmatrix} 0 \\ \hat{j} \end{pmatrix}.$$

For the stability analysis, we may neglect the source term and thus arrive at the two-by-two stability test model

$$\begin{pmatrix} \hat{u}' \\ \hat{v}' \end{pmatrix} = \begin{pmatrix} 0 & 1 \\ -\lambda & -\gamma \end{pmatrix} \begin{pmatrix} \hat{u} \\ \hat{v} \end{pmatrix}, \qquad \lambda \geq 0, \quad \gamma \geq 0. \quad (16)$$

The attractive feature of this formulation is that stability for the test model (16) induces stability for (11) in the norm generated by the inner product in (12).

Useful though equation (16) is, it is important to emphasise that the derivation of (16) requires constant scalars in the coefficients ε_{r} and σ, thus limiting the generality of this approach.

4. Time-integration methods

Probably the most popular time-integration methods to use in combination with high-order DG methods are high-order Runge-Kutta methods, giving rise to what are collectively called the Runge-Kutta DG (RKDG) methods [5]. For continuous and $H(\text{curl})$-conforming FEMs geometric integrators are also widely used thanks to their ability to conserve symplecticity[2] at the discrete level [18]. In this section, we briefly recall the construction of these two families of methods and we also discuss local and global Richardson extrapolation.

The highest-order polynomial we use within the finite element methods is $p = 3$. For both the DG and the $H(\text{curl})$-conforming methods, this corresponds to fourth-order convergence for the semi-discrete system (2) provided that the solution is smooth [13, 14, 11, 12]. Therefore, we now only discuss time-integration methods that are also at most fourth-order accurate. Extension to higher order, however, is usually straightforward.

For investigating the properties of any given time-integration method, let τ denote the time-step size and introduce $z_\lambda = \tau\sqrt{\lambda}$ and $z_\gamma = \tau\gamma$.[3] The stability of the time-integration method can then, in general, be best inspected through the (numerically determined) stability region

$$\mathcal{S} = \{(z_\lambda, z_\gamma) : z_\lambda, z_\gamma \geq 0 \ \text{ with } \ |\mu| < 1, \ \mu \text{ eigenvalues of the amplification operator}\}$$

associated with the test model (16).

4.1. Runge-Kutta methods

Out of the many different types of Runge-Kutta methods, strong-stability-preserving Runge-Kutta methods (SSPRK) [5] are particularly well suited for the time integration of semi-discrete hyperbolic problems.

With the definition of the initial values $U_0 = u_n$ and $V_0 = v_n$ for the time step from t_n to t_{n+1}, the general s-stage SSPRK scheme for (11) reads

$$\begin{aligned} U_k &= \sum_{l=0}^{k-1} \left(\alpha_{kl} U_l + \tau\beta_{kl} V_l\right), \\ M_\varepsilon V_k &= \sum_{l=0}^{k-1} \left(\alpha_{kl} V_l + \tau\beta_{kl}\left(-S_\mu U_l - M_\sigma V_l + j(t_l)\right)\right), \\ u_{n+1} &= U_s, \\ v_{n+1} &= V_s, \end{aligned} \tag{17}$$

where $k = 1, \ldots, s$ while α_{kl} and β_{kl} are the coefficients in the SSPRK method. Applying (17) to the test equation (16), the amplification operator $\mathcal{M}^s_{\text{ssp}}$ of an s-stage SSPRK method is

$$\mathcal{M}^k_{\text{ssp}} = \sum_{l=1}^{k-1} \mathcal{B}_{kl} \mathcal{M}^{l-1}_{\text{ssp}} \qquad \text{with} \qquad \mathcal{B}_{kl} = \alpha_{kl} \begin{pmatrix} 1 & 0 \\ 0 & 1 \end{pmatrix} + \beta_{kl} \begin{pmatrix} 0 & 1 \\ z_\lambda^2 & -z_\gamma \end{pmatrix}, \tag{18}$$

where, again, $k = 1, \ldots, s$ and $\mathcal{M}^0_{\text{ssp}}$ is the identity. We show the stability regions of several SSPRK schemes in Figure 2, where we refer to an s-stage pth-order SSPRK method as SSPRK(s,p). It is important to emphasise that any (standard as well as 'nonstandard' such as SSP) explicit s-stage pth-order RK methods with $s = p$ has the same amplification matrix. In those cases the choice of coefficients only determines the SSP property and not the shape of the stability region. For the cases when $s = p+1$, we display the stability regions of the methods that were derived and analysed in [28, 29, 30]. The plots suggest that increasing the number of stages, while keeping the polynomial order fixed, results in

[2] The preservation of symplecticity is important because it is related to energy. More precisely, for symplectic integrators the error in total energy will remain within a certain margin throughout the entire time integration.

[3] These values appear in a natural way in the amplification matrices of most time-integration methods described later in this section.

a more favourable time-step restriction for the conduction part – one that more than offsets the cost of introducing an additional stage at each time step. This is in line with known results for the linear advection equation [28, 29]. Nevertheless, explicit SSPRK methods treat the conduction term, as well as the wave term, explicitly, which entails a time-step condition that is too restrictive even for moderately conductive materials (see next section). Note that the second-order methods are only stable for $z_\gamma > 0$, i.e. for $\sigma > 0$.

4.2. Composition methods

Composition methods [31, 32, 33] are especially suitable for geometric integration [18] and thus for the time integration of first-order Hamiltonian systems. Our description of the composition methods here strictly follows that in [17] and we refer to that work for more details.

The second-order composition method for (11) is defined as

$$\begin{aligned} \frac{u_{n+1/2} - u_n}{\tau} &= \frac{1}{2} v_n, \\ M_\varepsilon \frac{v_{n+1} - v_n}{\tau} &= -S_\mu u_{n+1/2} - \frac{1}{2} M_\sigma (v_n + v_{n+1}) + \frac{1}{2} \left(j(t_n) + j(t_{n+1}) \right), \\ \frac{u_{n+1} - u_{n+1/2}}{\tau} &= \frac{1}{2} v_{n+1}, \end{aligned} \tag{19}$$

which is akin to the ubiquitous leapfrog scheme, with the only difference being in the treatment of the source term (cf. [34]). If applied to the test model (16), it has the amplification matrix

$$\mathcal{M}_{\mathrm{co2}} = \begin{pmatrix} 1 - \frac{1}{2} z_\lambda^2 + \frac{1}{2} z_\gamma & 1 - \frac{1}{4} z_\lambda^2 \\ -z_\lambda^2 & 1 - \frac{1}{2} z_\lambda^2 - \frac{1}{2} z_\gamma \end{pmatrix}, \tag{20}$$

which entails the stability properties: $z_\lambda \leq 2$ if $z_\gamma = 0$ and $z_\lambda < 2$ if $z_\gamma > 0$. An attractive feature of this method over explicit RK methods is that it is unconditionally stable with respect to the conduction term.

In principle, it is possible to construct an arbitrary high-order composition method [31]. In this article, however, we are only interested in at most fourth-order accurate methods so we will now only discuss the fourth-order composition method. We define the initial values for the inner time step as $U_0 = u_n$ and $V_0 = v_n$, time levels t^u, t^v for u, v and coefficients

$$\begin{aligned} &\beta_0 = \alpha_0 = 0, \quad \beta_1 = \alpha_5 = \tfrac{14 - \sqrt{19}}{108}, \quad \beta_2 = \alpha_4 = \tfrac{-23 - 20\sqrt{19}}{270}, \\ &\beta_3 = \alpha_3 = \tfrac{1}{5}, \quad \beta_4 = \alpha_2 = \tfrac{-2 + 10\sqrt{19}}{135}, \quad \beta_5 = \alpha_1 = \tfrac{146 + 5\sqrt{19}}{540}. \end{aligned}$$

The fourth-order composition method [31, 32, 17] for (11) now reads

$$\begin{aligned} \frac{U_k - U_{k-1}}{\tau} &= (\beta_k + \alpha_{k-1}) V_{k-1}, \\ M_\varepsilon \frac{V_k - V_{k-1}}{\tau} &= \beta_k \left(-S_\mu U_k - M_\sigma V_{k-1} + j(t_{k-1}^v) \right) + \alpha_k \left(-S_\mu U_k - M_\sigma V_k + j(t_k^v) \right), \\ v_{n+1} &= V_s, \\ u_{n+1} &= U_s + \alpha_s \tau V_s, \end{aligned} \tag{21}$$

where $k = 1, \ldots, s$, $s = 5$ is the number of internal time levels, and $t_k^v = t_n + (\tilde{\alpha}_k + \tilde{\beta}_k)\tau$ and $t_k^u = t_n + (\tilde{\alpha}_{k-1} + \tilde{\beta}_k)\tau$ with the coefficients $\tilde{\alpha}_k = \alpha_1 + \cdots + \alpha_k$ and $\tilde{\beta}_k = \beta_1 + \cdots + \beta_k$.

The amplification operator of (21) when applied to (16) is then

$$\prod_{k=5}^{1} \frac{1}{1 + \alpha_k z_\gamma} \begin{pmatrix} 1 + \alpha_k z_\gamma & (1 + \alpha_k z_\gamma)(\alpha_{k-1} + \beta_k) \\ -(\alpha_k + \beta_k) z_\lambda^2 & 1 - \beta_k z_\gamma - (\beta_k + \alpha_{k-1})(\beta_k + \alpha_k) z_\lambda^2 \end{pmatrix}. \tag{22}$$

An important property of any fourth-order composition method is that it inevitably contains a negative coefficient, which in our case is $\alpha_4 = \beta_2$. This entails a stability restriction that is conditional even for an implicitly treated conduction term. This is illustrated in Figure 3, where parts of the upper right

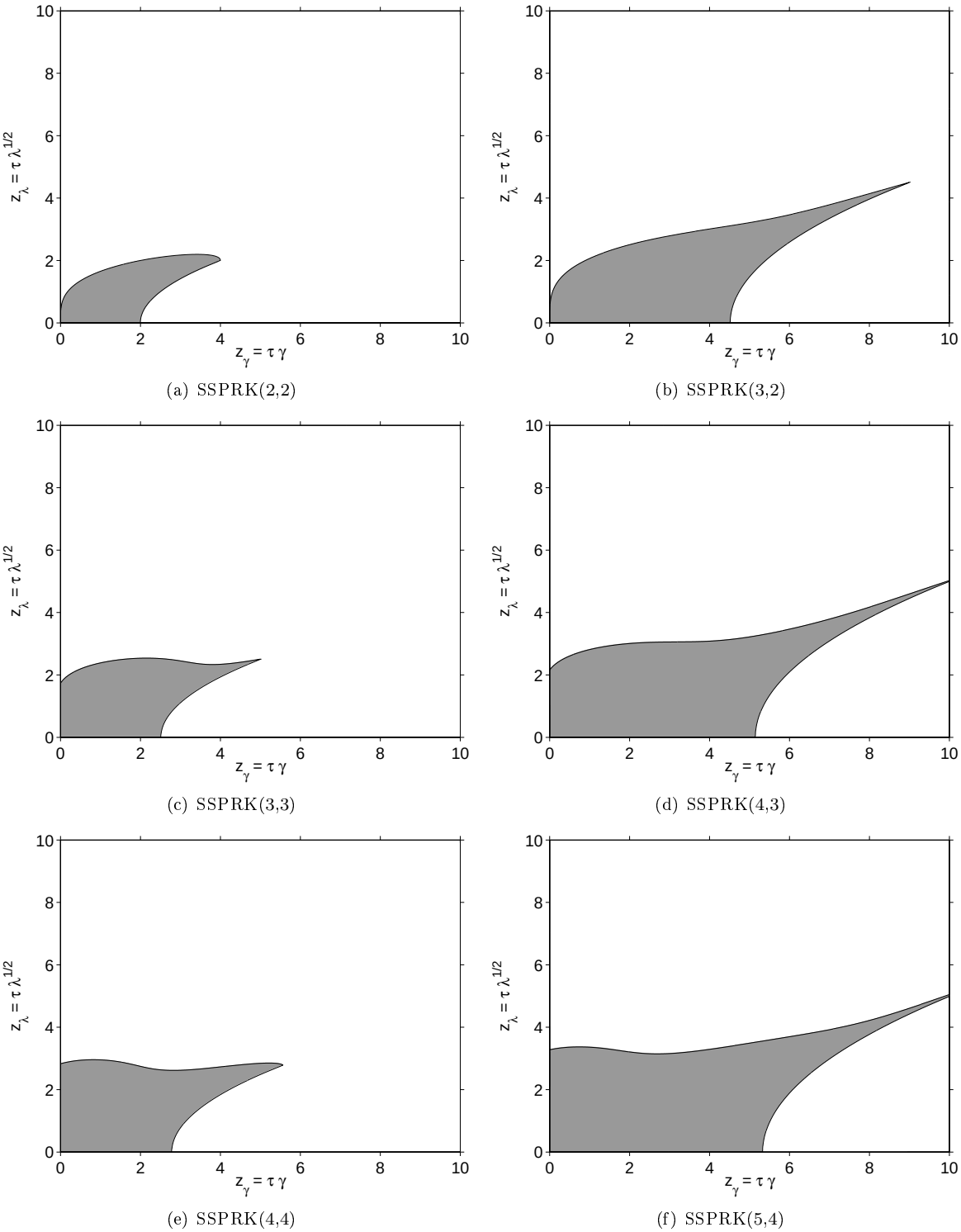

(a) SSPRK(2,2)

(b) SSPRK(3,2)

(c) SSPRK(3,3)

(d) SSPRK(4,3)

(e) SSPRK(4,4)

(f) SSPRK(5,4)

Figure 2: Stability regions (shaded areas) for several explicit SSPRK(s,p) methods, where s is the number of stages and p is the order of the method. Note that all explicit RK methods with $s = p$ have the same stability regions as SSPRK(s,p) with $s = p$ (left column).

half of the stability region for (21) is shown. Stability is guaranteed as long as $z_\gamma < 2.4$ and $z_\lambda < 3$, or equivalently, if $\tau < 2.4/\gamma$ and $\tau < 3/\sqrt{\lambda}$.

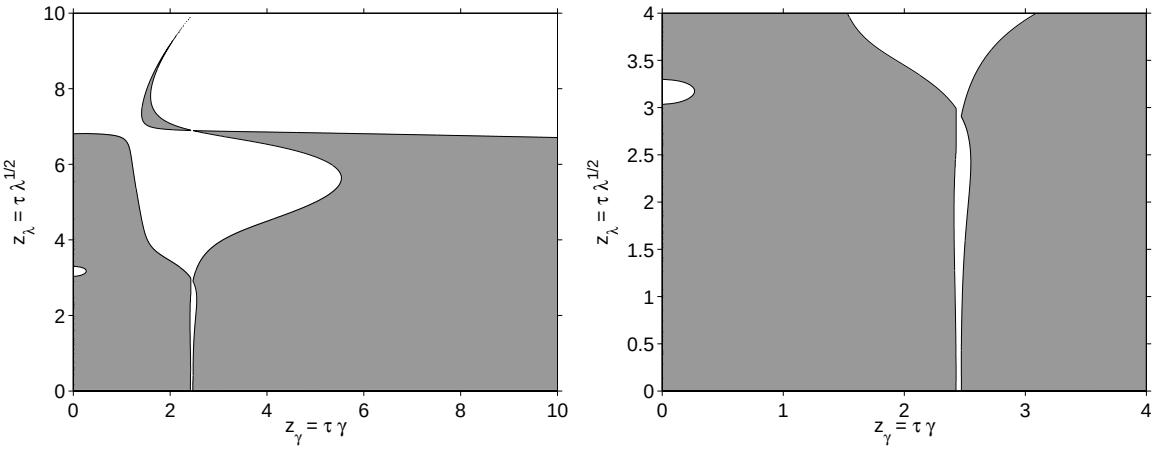

Figure 3: Stability region (shaded area) of the fourth-order composition method. The right plot zooms in on the region where stability is guaranteed. (Cf. Figure 5.1 in [17].)

4.3. Fourth-order global Richardson extrapolation

As already mentioned in the previous section, when $\sigma > 0$ the stability condition may be very restrictive even for moderately conductive materials. In these cases, high-order composition methods and SSPRK methods are not competitive. Instead, one would prefer to use explicit methods which treat the conduction term in an unconditionally stable manner. Since the second-order composition method is such a method, extending it to higher order through Richardson extrapolation is an obvious alternative. We refer to [17] for a detailed discussion on the stability properties of the fourth-order local and global versions of the Richardson extrapolation. Here we first recall the construction of the fourth-order global Richardson extrapolation (GEX4)

$$u_\tau^{\mathrm{gex4}} = \frac{4}{3}u_{\frac{\tau}{2}}^{\mathrm{co2}} - \frac{1}{3}u_\tau^{\mathrm{co2}}, \tag{23}$$

where $u_{\frac{\tau}{2}}^{\mathrm{co2}}$ and u_τ^{co2} denote the results at final time computed by the second-order composition method with time steps $\frac{\tau}{2}$ and τ, respectively. Since extrapolation only takes place once at the final time of the integration, this method has the same stability properties as the second-order composition method. Note that it only needs three times as much computational work per time step.

For long time integration and in the absence of damping, global extrapolation may not be sufficiently effective in annihilating leading error terms. In these cases, the local version of Richardson extrapolation – when the extrapolation is performed at each time step – is usually more beneficial. The local version of (23) is, however, not unconditionally stable with respect to z_γ. Instead, we can use the fourth-order local extrapolation (LEX4) defined as

$$u_\tau^{\mathrm{lex4}} = \frac{9}{8}u_{\tau/3}^{\mathrm{co2}} - \frac{1}{8}u_\tau^{\mathrm{co2}}, \tag{24}$$

where the work per time step is approximately four times as much as that of CO2. The amplification operator of LEX4 for the test model (16) reads

$$\frac{9}{8}\mathcal{M}_{\mathrm{co2}}^3(z_\lambda/3, z_\gamma/3) - \frac{1}{8}\mathcal{M}_{\mathrm{co2}}(z_\lambda, z_\gamma), \tag{25}$$

where $\mathcal{M}_{\mathrm{co2}}(z_\lambda, z_\gamma)$ denotes the amplification operator (20) of CO2. Figure 4 shows the associated stability region $\mathcal{S}$, which indicates an approximate stability interval $0 \le z_\lambda \le 2.85$ and unconditional stability for z_γ.

5. Numerical experiments

In this section, we perform numerical tests to establish the convergence rates of the fully discrete systems that result from the spatial and time discretisations described in the previous two sections. We

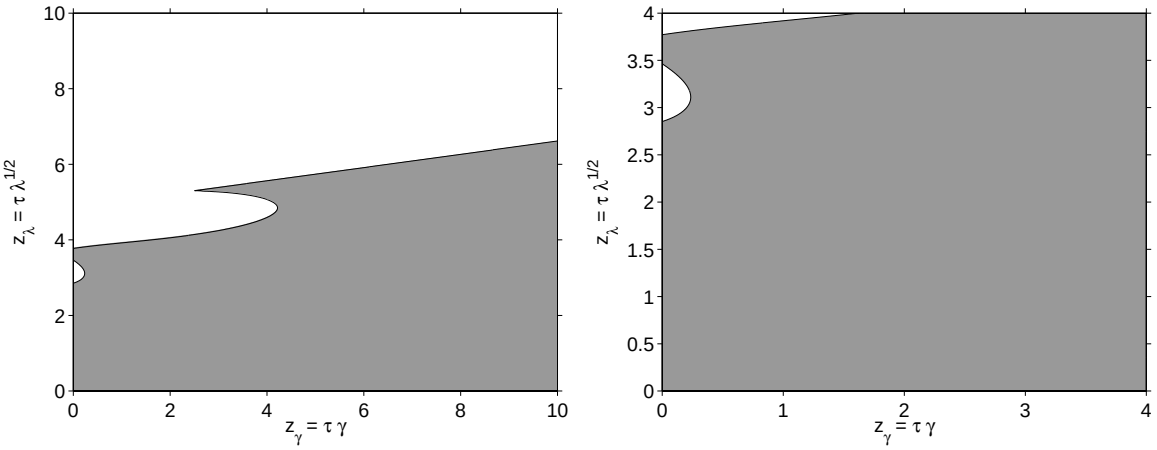

Figure 4: Stability region (shaded area) of the fourth-order local Richardson extrapolation (24). The right plot zooms in on the region where stability for wave term z_λ is guaranteed. Stability for the conduction term z_γ is unconditional.

also carry out a numerical dispersion analysis of the semi- and fully discrete system with DG spatial discretisation. This is done in the following way: *i)* solve the time-harmonic eigenvalue problem, which corresponds to the semi-discrete system with Fourier mode initial conditions; *ii)* apply a chosen time-integration method to the test model (16) with the computed semi-discrete numerical frequency. This approach has two main advantages over simply solving the eigenvalue problem that results from applying the amplification matrix directly to (11). First, it is more efficient because we solve an eigenvalue problem that is smaller and always symmetric. Second, it makes it possible to study the dispersion (and dissipation) properties of the time-integration scheme separately from those of the semi-discrete scheme.

5.1. Convergence and comparison of performance

We use a simple test example to illustrate the numerical performance of the two spatial discretisation techniques described in Section 2. For both methods, the predicted convergence rate of the semi-discrete system is $\mathcal{O}(h^{p+1})$ in the $L^2(\Omega)$ norm and $\mathcal{O}(h^p)$ in the energy norm for smooth solutions; see for example [12, 35, 25, 13, 14]. It is thus natural to choose the time-integration method such that it guarantees at least the same order of convergence. Therefore, if the polynomial order in the FEM is at most one we use the second-order composition method; if the polynomial order is two or three we apply one of the possible fourth-order methods described in Section 4.

The numerical tests are implemented in *hp*GEM[4] [36], a general finite element package suitable for solving a variety of physical problems in fluid dynamics and electromagnetism. To integrate the semi-discrete system in time we use PETSc [37], which is particularly efficient in computing matrix-vector multiplications and solving linear systems for large sparse matrices. As a stopping criterion in the linear solver for the $H(\mathrm{curl})$-conforming method, we set the tolerance at $\texttt{tol} = 10^{-8}$.

In the example, we consider (1) in the cubic domain $\Omega = (0,1)^3$. We define the time-independent field

$$\bar{\boldsymbol{E}}(x,y,z) = \begin{pmatrix} \sin(\pi y)\sin(\pi z) \\ \sin(\pi z)\sin(\pi x) \\ \sin(\pi x)\sin(\pi y) \end{pmatrix}$$

and choose the source term to be

$$-\frac{\partial \boldsymbol{J}}{\partial t} = \left(\varepsilon_{\mathrm{r}}\eta''(t) + \sigma\eta'(t) + 2\pi^2\eta(t)\right)\bar{\boldsymbol{E}}(x,y,z).$$

[4] The software is free to download and available at `http://wwwhome.math.utwente.nl/~hpgemdev/download.php`.

Thus the exact solution reads

$$\boldsymbol{E}(t,x,y,z) = \eta(t)\bar{\boldsymbol{E}}(x,y,z), \quad \eta(t) = \sum_{k=1}^{3} \cos \omega_k t, \tag{26}$$

with $\omega_1 = 1$, $\omega_2 = 1/2$, $\omega_3 = 1/3$, $\varepsilon_\mathrm{r} = 1$. We either set $\sigma = 0$ or $\sigma = 60\pi$, and we integrate until final time $T_\mathrm{end} = 12\pi$ (exactly one time period).

When the globally $H(\mathrm{curl})$-conforming discretisation [12, 11] is used, we need to solve a linear system at each time step. Since the matrix M_ε is positive definite, a natural choice of linear solver is the preconditioned conjugate gradient (PCG) method. For simplicity, we apply the incomplete Cholesky preconditioner for all meshes and polynomial orders. We emphasise that preconditioning is not an issue for the DG method since we can simply invert the block-diagonal mass matrix at negligible cost.

As a first example, we run (26) with $\sigma = 0$ and final time $T_\mathrm{end} = 12\pi$, on a sequence of structured meshes with $N_\mathrm{el} = 5, 40, 320, 2560, 20480, 163840$ elements. In each mesh the largest face diameter h is exactly half that of the previous mesh. We plot the convergence rates in Figure 5 in both the $L^2(\Omega)$-norm and the energy norm for polynomial orders $p = 1, 2, 3$. Note that the convergence is shown as a function of degrees of freedom, which is equivalent to showing the convergence as function of $1/h$ in the DG case. However, in the $H(\mathrm{curl})$-conforming case there is some difference between the two, as the number of degrees of freedom generally increase slightly more than eightfold when h is halved. Nevertheless, we can see that the expected convergence rates are achieved asymptotically for both the DG and the $H(\mathrm{curl})$-conforming methods. We can also observe that it takes fewer degrees of freedom for the $H(\mathrm{curl})$-conforming discretisation to reach a given accuracy. Furthermore, we can confirm the well-established observation that the use of high-order approximations pays off (at least for smooth solutions) in terms of accuracy per degrees of freedom.

To gain further insight into the computational costs of the time integration, we show the performance of the DG method in Tables I and III; and that of the $H(\mathrm{curl})$-conforming method in Tables II and IV. In this particular example, we use a structured mesh with 320 elements and an unstructured one with 432 elements.[5] Although the accuracy of the two methods is comparable, the computational costs are not and the pattern changes dramatically as the order increases. The total number of matrix-vector multiplications (matvecs) needed to integrate until T_end is always higher for the $H(\mathrm{curl})$-conforming case than for the DG method. This is not surprising given that at each time step a linear system has to be solved. However, this seemingly unfavourable property does not manifests itself in longer computational time for $p = 1$ and $p = 2$ on structured meshes, thanks in part to the smaller size of the system and in part to a weaker time-step restriction in the $H(\mathrm{curl})$-conforming FEM. The situation is different for $p = 3$. Here, the increased number of matvecs translates readily into more CPU time on both structured and unstructured meshes. This is partly because of a trade-off between the conditioning of the mass matrix and the use of the hierarchic basis. Mass matrices based on hierarchic bases tend to be relatively badly conditioned. This does not influence the performance of the DG method. But it renders the $H(\mathrm{curl})$-conforming method less effective because the number of iterations in solving the linear system at each time step grows significantly with the polynomial order. This effect is even more pronounced on unstructured meshes, where DG performs slightly better for $p = 2$ already and where the $H(\mathrm{curl})$-conforming computation for $p = 3$ is excessively long – which is one reason why we only completed one of them.

The choice of the time-integration method does not influence the computational results much in this example. Nevertheless, LEX4 appears to be the most efficient thanks to the balance between the allowable time-step size and the computational work needed per time step. We also note that for this particular mesh the use of fourth-order time-integration methods may not be necessary even for $p = 2, 3$. This is solely because the spatial error is not yet in the asymptotic regime and therefore dominates. We take a closer look at this shortly in terms of numerical dispersion and dissipation.

On structured meshes, we repeat example (26) with conductivity $\sigma = 60\pi$, which corresponds to the dimensional value $\tilde{\sigma} = 0.5\,\mathrm{S\,m^{-1}}$, typical of the human abdomen. The convergence results are shown in

[5] A mesh of 320 or 432 tetrahedra is sufficient to compare the different methods from the point of view of accuracy and computational work. A finer mesh would naturally give a more accurate solution but the relative performance of the methods would remain the same.

Table I: Computational costs of the DG method for example (26) with $\sigma = 0$. A structured mesh of 320 elements is used with spatial polynomial orders $p = 1, 2, 3$.

	method	# DoF	$L^2(\Omega)$ error	# matvecs	τ	CPU time
$p = 1$	CO2	3840	1.2174e-01	4526	0.0167	8s
$p = 2$	CO2	9600	1.1696e-02	7542	0.0100	114s
$p = 2$	GEX4	9600	1.2303e-02	22624	0.0100	342s
$p = 3$	CO4	19200	7.0432e-04	35192	0.0107	2013s
$p = 3$	GEX4	19200	9.0148e-04	31672	0.0071	1863s
$p = 3$	LEX4	19200	6.1762e-04	28154	0.0107	1623s

Table II: Computational costs of the $H(\text{curl})$-conforming method for example (26) with $\sigma = 0$. A structured mesh of 320 elements is used with spatial polynomial orders $p = 1, 2, 3$.

	method	# DoF	$L^2(\Omega)$ error	# matvecs	τ	CPU time
$p = 1$	CO2	504	2.7283e-01	7783	0.0417	2s
$p = 2$	CO2	2388	1.3642e-02	59201	0.0250	87s
$p = 2$	GEX4	2388	1.2942e-02	180067	0.0250	264s
$p = 3$	CO4	6640	7.4117e-04	817880	0.0268	19683s
$p = 3$	GEX4	6640	7.7523e-04	736276	0.0179	17492s
$p = 3$	LEX4	6640	8.5234e-04	653611	0.0268	15510s

Table III: Computational costs of the DG method for example (26) with $\sigma = 0$. An unstructured mesh of 432 elements is used with spatial polynomial orders $p = 1, 2, 3$.

	method	# DoF	$L^2(\Omega)$ error	# matvecs	τ	CPU time
$p = 1$	CO2	5184	1.9583e-01	11878	0.00635	41s
$p = 2$	CO2	12960	1.3396e-02	19796	0.00381	429s
$p = 2$	GEX4	12960	1.4316e-02	59384	0.00381	1263s
$p = 3$	CO4	25920	1.4311e-03	92372	0.00408	7585s
$p = 3$	GEX4	25920	1.5558e-03	83134	0.00272	6749s
$p = 3$	LEX4	25920	1.4038e-03	73898	0.00408	5909s

Table IV: Computational costs of the $H(\text{curl})$-conforming method for example (26) with $\sigma = 0$. An unstructured mesh of 432 elements is used with spatial polynomial orders $p = 1, 2, 3$.

	method	# DoF	$L^2(\Omega)$ error	# matvecs	τ	CPU time
$p = 1$	CO2	744	1.9113e-01	33691	0.02380	18s
$p = 2$	CO2	3420	1.7294e-02	169129	0.01429	963s
$p = 2$	GEX4	3420	1.8860e-02	406784	0.01429	2778s
$p = 3$	CO4	9360	—	>1e+07	0.01530	>5e+05s
$p = 3$	GEX4	9360	1.9676e-03	21337490	0.01020	782647s
$p = 3$	LEX4	9360	—	>1e+07	0.01530	>5e+05s

Figure 6, from which it appears that they are similar to the nonconductive case except that optimal rates of convergence are reached sooner. On unstructured meshes, the example is repeated with conductivity $\sigma = 450\pi$, a value more typical of seawater. See Table V for the conductivity of a small selection of materials (source: `en.wikipedia.org/wiki/Electrical_conductivity`).

The computational work, depicted in Tables VI–IX, also shows a similar pattern to the conduction-free case, except when the fourth-order composition method is used. In that case, the conduction term poses a stricter time-step size than the wave term and increases the number of time steps and thus the computational cost. On the structured mesh with 320 elements and $\sigma = 60\pi$, this only affects the

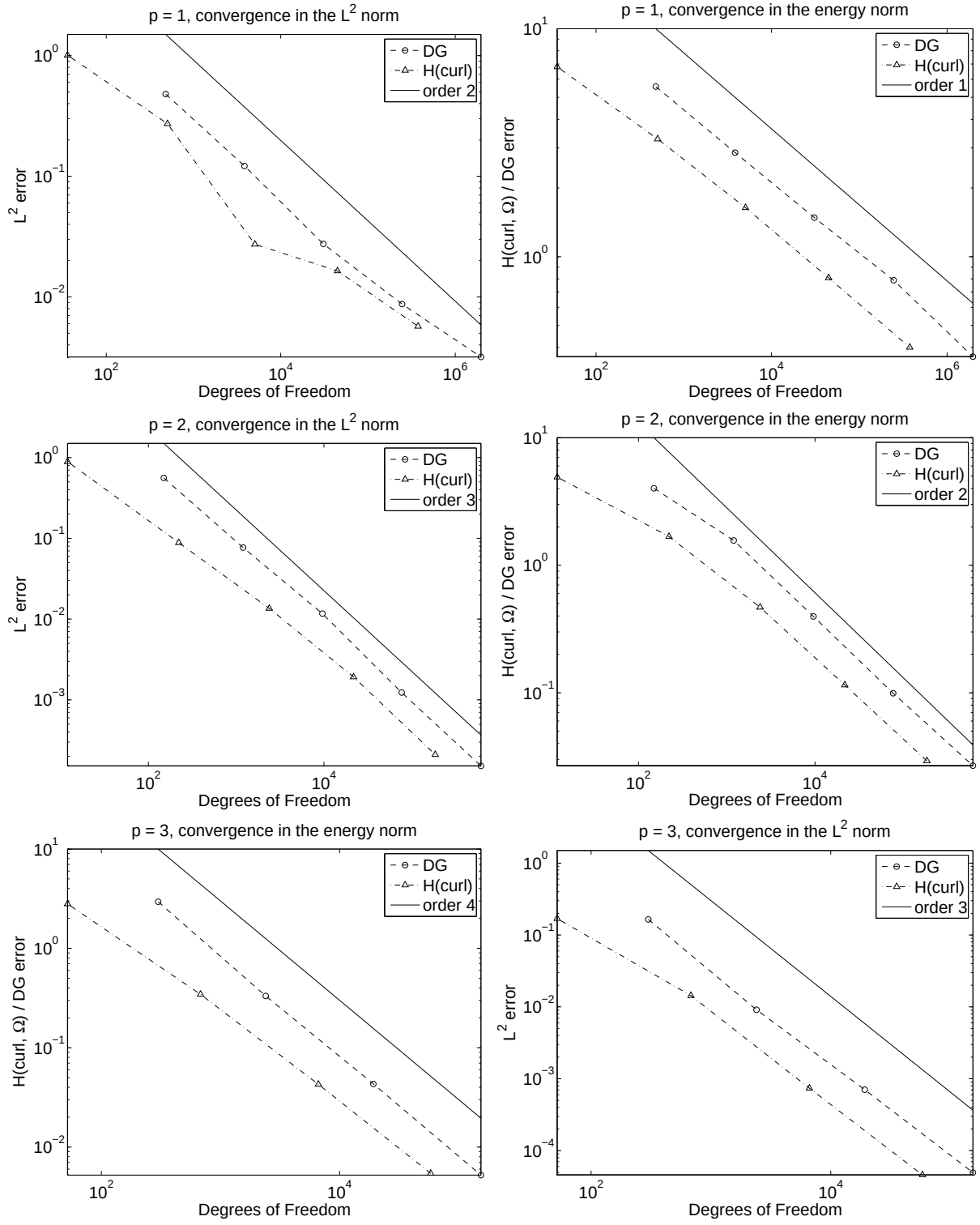

Figure 5: Convergence plots in the L^2-norm (left column) and in the energy norm (right column) for test example (26) with $\sigma = 0$. In each plot the convergence rates of the DG method and the $H(\mathrm{curl})$-conforming method are shown along with the expected order of convergence.

$H(\mathrm{curl})$-conforming discretisation because the stiffness matrix in the DG method has a significantly larger spectral radius (and therefore it still determines the stability condition). On the unstructured mesh with

Table V: Electrical conductivity of some materials measured in Siemens per metre ($\mathrm{S\,m^{-1}}$). For the dimensionless value a multiplication by 120π is needed. Source: `en.wikipedia.org/wiki/Electrical_conductivity`.

Material	Conductivity ($\mathrm{S\,m^{-1}}$)	Note
Silver	63.0e+06	Best electrical conductor
Copper	59.6e+06	
Gold	45.2e+06	Commonly used in electrical contacts
Aluminium	37.8e+06	
Seawater	4.8	For average salinity of 35 g/kg
Human Body	0.006–1.5	Varies from bone to cerebrospinal fluids
Drinking water	0.0005–0.05	
Deionised water	5.5e-06	Lowest value, with monoatomic gases present
Air	5e-15	Varies slightly depending on humidity

432 elements and $\sigma = 450\pi$, however, it already affects the DG discretisation too. This indicates that large values of σ prohibit the use of fourth-order (or, indeed, any high-order) composition methods, as well as explicit RK methods, such as SSPRK. Instead, Richardson extrapolation based on the second-order composition method may be used since they are unconditionally stable with respect to the conductivity term. Similarly to the conduction-free case we killed the $H(\mathrm{curl})$-conforming computations after almost six days – already significantly more than what the DG computations take.

Table VI: Computational costs of the DG method for example (26) with $\sigma = 60\pi$. A mesh of 320 elements is used with spatial polynomial orders $p = 1, 2, 3$.

	method	# DoF	$L^2(\Omega)$ error	# matvecs	τ	CPU time
$p = 1$	CO2	3840	6.6817e-02	4526	0.0167	8s
$p = 2$	CO2	9600	8.4244e-03	7542	0.0100	113s
$p = 2$	GEX4	9600	8.4243e-03	22624	0.0100	341s
$p = 3$	CO4	19200	5.5619e-04	35192	0.0107	2012s
$p = 3$	GEX4	19200	5.5612e-04	31672	0.0071	1864s
$p = 3$	LEX4	19200	5.5612e-04	28154	0.0107	1623s

Table VII: Computational costs of the $H(\mathrm{curl})$-conforming method for example (26) with $\sigma = 60\pi$. A mesh of 320 elements is used with spatial polynomial orders $p = 1, 2, 3$.

	method	# DoF	$L^2(\Omega)$ error	# matvecs	τ	CPU time
$p = 1$	CO2	504	1.1789e-01	6253	0.0417	1s
$p = 2$	CO2	2388	1.2315e-02	56301	0.0250	82s
$p = 2$	GEX4	2388	1.2314e-02	166303	0.0250	247s
$p = 3$	CO4	6640	7.3357e-04	1717157	0.0127	40862s
$p = 3$	GEX4	6640	7.3358e-04	734732	0.0179	17472s
$p = 3$	LEX4	6640	7.3358e-04	653024	0.0268	15498s

5.2. Numerical dispersion analysis

To investigate the dispersion and dissipation properties of the fully discrete schemes, we consider the semi-discrete system (11) with $\sigma = 0$ and $j = 0$,

$$\begin{pmatrix} u' \\ v' \end{pmatrix} = \mathcal{A} \begin{pmatrix} u \\ v \end{pmatrix} \quad \text{with} \quad \mathcal{A} = \begin{pmatrix} 0 & I \\ -M_\varepsilon^{-1} S_\mu & 0 \end{pmatrix}, \tag{27}$$

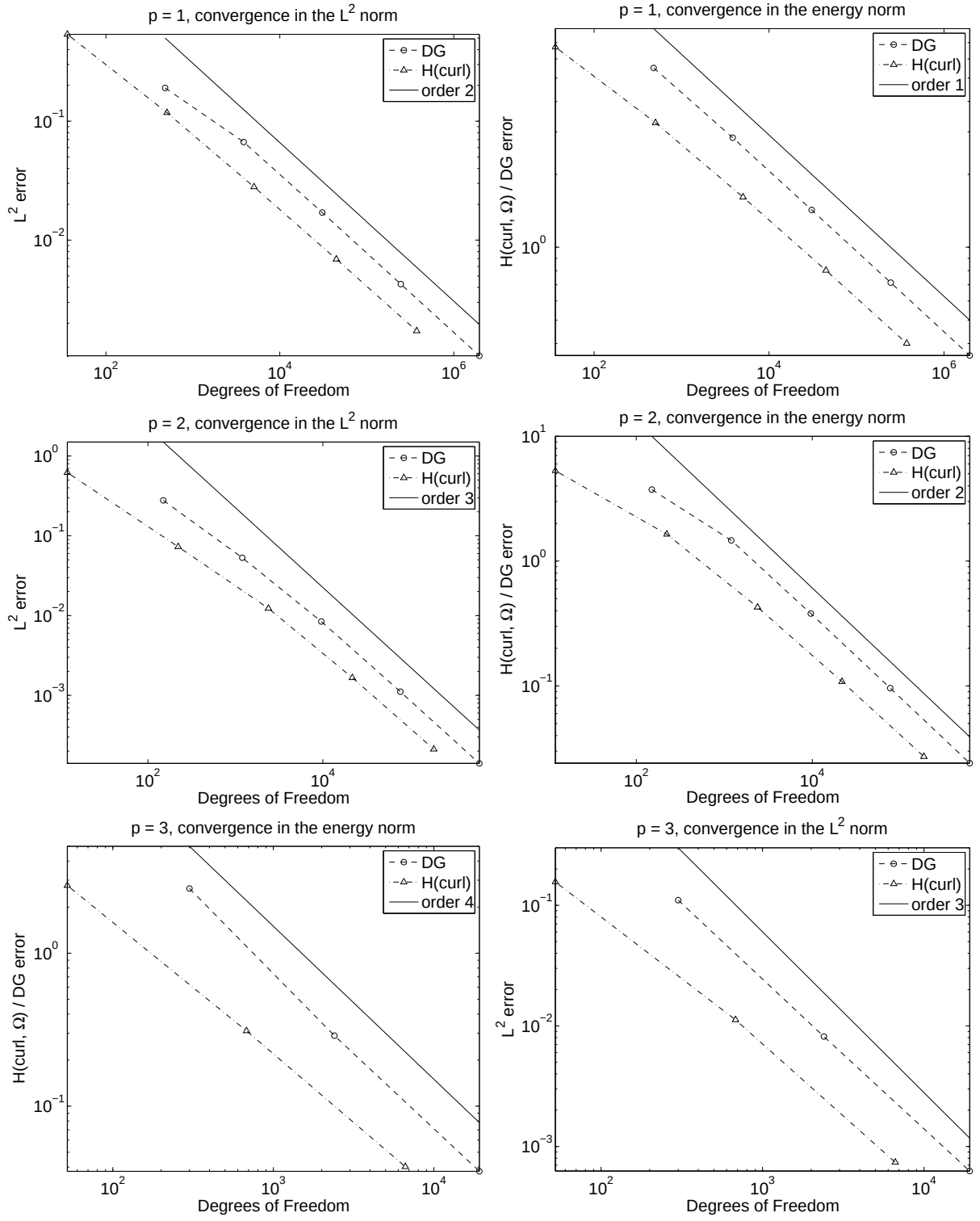

Figure 6: Convergence plots in the L^2-norm (left column) and in the energy norm (right column) for test example (26) with $\sigma = 60\pi$. In each plot the convergence rates of the DG method and the $H(\mathrm{curl})$-conforming method are shown along with the expected order of convergence.

and assume a plane wave exact solution

$$\boldsymbol{E}(\boldsymbol{x}, t) = \hat{\boldsymbol{E}} \exp(-\mathrm{i}\omega t) \exp(\mathrm{i}\boldsymbol{k} \cdot \boldsymbol{x}) \tag{28}$$

Table VIII: Computational costs of the DG method for example (26) with $\sigma = 450\pi$. An unstructured mesh of 432 elements is used with spatial polynomial orders $p = 1, 2, 3$.

	method	# DoF	$L^2(\Omega)$ error	# matvecs	τ	CPU time
$p = 1$	CO2	5184	4.6168e-02	11878	0.00635	41s
$p = 2$	CO2	12960	8.1650e-03	19796	0.00381	422s
$p = 2$	GEX4	12960	8.1650e-03	59384	0.00381	1240s
$p = 3$	CO4	25920	8.5690e-04	222072	0.00170	17606s
$p = 3$	GEX4	25920	8.5671e-04	83134	0.00272	6618s
$p = 3$	LEX4	25920	8.5690e-04	73898	0.00136	5906s

Table IX: Computational costs of the $H(\mathrm{curl})$-conforming method for example (26) with $\sigma = 450\pi$. An unstructured mesh of 432 elements is used with spatial polynomial orders $p = 1, 2, 3$.

	method	# DoF	$L^2(\Omega)$ error	# matvecs	τ	CPU time
$p = 1$	CO2	744	1.2498e-01	32049	0.02380	17s
$p = 2$	CO2	3420	1.3102e-02	163451	0.01429	938s
$p = 2$	GEX4	3420	1.3102e-02	490287	0.01429	2677s
$p = 3$	CO4	9360	—	>1e+07	0.01530	>5e+05s
$p = 3$	GEX4	9360	—	>1e+07	0.01020	>5e+05s
$p = 3$	LEX4	9360	—	>1e+07	0.01530	>5e+05s

with periodic boundary conditions and $\hat{\boldsymbol{E}} = \mathbf{1}$. In (28), $\mathrm{i}^2 = -1$, ω denotes the angular frequency, $k = (k_x, k_y, k_z)^T$ is the wave number. Between these quantities the (exact) dispersion relation $\omega^2 = k^2/c^2$ holds with $k^2 = k_x^2 + k_y^2 + k_z^2$ and with $c = 1/\left(\varepsilon_\mathrm{r}\mu_\mathrm{r}\right)^{1/2}$, which is the speed of light.

As a first step, we project the exact initial conditions $\boldsymbol{E}(\boldsymbol{x}, 0)$ and $\partial_t \boldsymbol{E}(\boldsymbol{x}, 0)$ onto the finite-element space

$$\begin{aligned} E_h^j(0) &= \left(\boldsymbol{E}(\boldsymbol{x}, 0), \boldsymbol{\psi}_j\right)_\Omega, \qquad j = 1 \dots N, \\ \frac{\mathrm{d}}{\mathrm{d}t} E_h^j(0) &= \left(\partial_t \boldsymbol{E}(\boldsymbol{x}, 0), \boldsymbol{\psi}_j\right)_\Omega, \qquad j = 1 \dots N. \end{aligned} \tag{29}$$

We can now obtain the initial conditions for (27) through the relations $u_0 = u(0) = M_{\varepsilon_\mathrm{r}}^{-1} E_h(0)$ and $v_0 = v(0) = u'(0) = M_{\varepsilon_\mathrm{r}}^{-1} \frac{\mathrm{d}}{\mathrm{d}t} E_h(0)$. The time-exact discrete Fourier mode at time level $n\tau$ is then defined as

$$\begin{pmatrix} u_n \\ v_n \end{pmatrix} = \nu^n \begin{pmatrix} u_0 \\ v_0 \end{pmatrix} \quad \text{with} \quad \nu^n = \mathrm{e}^{-\mathrm{i}\omega_h n\tau}, \tag{30}$$

where ν^n is the exact amplification factor and ω_h is the semi-discrete numerical frequency.

To first see the impact of the space discretisation only, we consider the semi-discrete equation

$$M_\varepsilon u'' + S_\mu u = 0 \tag{31}$$

with periodic boundary conditions and a plane wave initial condition (28). In this case, (31) is equivalent to the discrete time-harmonic Maxwell eigenvalue problem

$$S_\mu u - \omega_h^2 M_\varepsilon u = 0 \tag{32}$$

with periodic boundary conditions. All semi-discrete eigenvalues ω_h^2 of (32) are real and non-negative, which entails that the space discretisation imposes no dissipation. In Table X, we show the numerical frequencies of the spatial DG discretisation for the Fourier mode with $k_x = 2\pi, k_y = -2\pi, k_z = 0$, i.e. with exact angular frequency $\omega_\mathrm{ex} = \sqrt{8}\pi$. The number of elements for each mesh is $N_\mathrm{el} = 5(\frac{1}{h})^3$ and in each element the local number of degrees of freedom is $\frac{1}{2}(p+1)(p+2)(p+3)$. To solve the eigenvalue discrete

problem (32) of this size the `Matlab` implementation[6] of the Jacobi-Davidson iterative method [38, 39] is used. We note that for other Fourier modes the same approximation properties apply as long as $\omega_h h$ is in the same region as shown in the tables. The frequency errors for the same meshes and polynomial orders are depicted in Table XI. Note that the frequency errors are signed, indicating phase advance.

Table X: Semi-discrete frequencies ω_h of the DG method that approximate the exact frequency $\omega_{\text{ex}} = \sqrt{8}\pi$

	$h = \frac{1}{2}$	$h = \frac{1}{4}$	$h = \frac{1}{8}$	$h = \frac{1}{16}$	ω_{ex}
$p = 1$	—	9.4286	9.0469	8.9271	8.8858
$p = 2$	9.4738	8.9276	8.8887	—	8.8858
$p = 3$	8.9146	8.8875	8.8858	—	8.8858

Table XI: Frequency error $\omega_h - \omega_{\text{ex}}$ of the DG semi-discrete system with exact frequency $\omega_{\text{ex}} = \sqrt{8}\pi$

	$h = \frac{1}{2}$	$h = \frac{1}{4}$	$h = \frac{1}{8}$	$h = \frac{1}{16}$
$p = 1$	—	5.4283e-01	1.6117e-01	4.1380e-02
$p = 2$	5.8800e-01	4.1831e-02	2.9628e-03	—
$p = 3$	2.8869e-02	1.7173e-03	3.0850e-05	—

To include the time integration in the dispersion analysis it suffices to apply a chosen time-integration method to the test model (16) with $\gamma = 0$. We are allowed to do that because the eigenvalues of $\tilde{S}_\mu$ are the same as the eigenvalues of $M_\varepsilon^{-1} S_\mu$, that is $\lambda = \omega_h^2$. Let $\mathcal{M}$ denote the amplification operator of any of the time-integration methods described in Section 4. So instead of (30) we now have the fully discrete Fourier mode at time level $n\tau$,

$$\nu_h^{n+1} \begin{pmatrix} u_0 \\ v_0 \end{pmatrix} = \mathcal{M} \nu_h^n \begin{pmatrix} u_0 \\ v_0 \end{pmatrix}, \tag{33}$$

which reduces to the eigenvalue problem

$$\nu_h \begin{pmatrix} u_0 \\ v_0 \end{pmatrix} = \mathcal{M} \begin{pmatrix} u_0 \\ v_0 \end{pmatrix}. \tag{34}$$

Solving this eigenvalue problem will produce two eigenpairs, representing two waves with the same wave number but travelling in opposite directions. Without loss of generality, we can discard the one with negative real part and establish the dispersive and dissipative properties of the fully discrete scheme through the relation

$$\nu_h = \mathrm{e}^{-\mathrm{i}\omega_h^\tau \tau},$$

where ω_h^τ represents the fully discrete numerical frequency. The real part of ω_h^τ defines the actual angular frequency in the discrete dispersion relation, while a negative imaginary part indicates numerical dissipation. A non-negligible positive imaginary part would mean instability.

We show the frequency errors of the time-integration schemes SSPRK(4, 3), CO2 and LEX4 in Tables XII– XIV. They show that the frequency error of the time-integration method is at least an order smaller than the one of the DG method, as long as the order of the time-integration method is on a par with the order of the DG method. When this is not the case, such as when CO2 is used for $p = 2$ or $p = 3$, the frequency error of the time integration is commensurate with, or exceeds that of the DG discretisation.

Composition methods, such as CO2 and CO4, are known to be non-dissipative [31]. Thus combining them with a symmetric spatial discretisation results in an energy-conservative fully-discrete discretisation. Global Richardson extrapolation based on a composition method naturally inherits this property. However, local Richardson extrapolation may introduce a slight dissipation even when based on a non-dissipative scheme such as CO2. We show this in Table XV and note that the error is generally too

[6] The software is free to download and available at `http://www.math.uu.nl/people/sleijpen`.

small to have a real impact on simulations arising in practice. By comparison, the SSPRK(4, 3) scheme introduces a much more significant level of dissipation, shown in Table XVI.

Finally, we note that if a time-dependent boundary condition is used in (1) instead of a homogeneous one, order reduction may occur. See [17] for the possible effects of this.

Table XII: Frequency error imposed only by the time integration, $\mathrm{Re}(\omega_h^\tau) - \omega_h$, of the SSPRK(4, 3) method for semi-discrete numerical frequencies ω_h taken from Table X.

	$h = \frac{1}{2}$	$h = \frac{1}{4}$	$h = \frac{1}{8}$	$h = \frac{1}{16}$
$p = 1$	—	7.1799e-05	3.6525e-06	2.1360e-07
$p = 2$	1.5242e-04	7.0867e-06	4.3347e-07	—
$p = 3$	2.9293e-05	1.8039e-06	1.1265e-07	—

Table XIII: Frequency error imposed only by the time integration, $\mathrm{Re}(\omega_h^\tau) - \omega_h$, of the CO2 method for semi-discrete numerical frequencies ω_h taken from Table X.

	$h = \frac{1}{2}$	$h = \frac{1}{4}$	$h = \frac{1}{8}$	$h = \frac{1}{16}$
$p = 1$	—	9.7283e-03	2.1439e-03	5.1472e-04
$p = 2$	1.4229e-02	2.9674e-03	7.3172e-04	—
$p = 3$	6.0353e-03	1.4930e-03	3.7292e-04	—

Table XIV: Frequency error imposed only by the time integration, $\mathrm{Re}(\omega_h^\tau) - \omega_h$, of the LEX4 method for semi-discrete numerical frequencies ω_h taken from Table X. The negative values indicate that the frequency error caused by the time integration counteracts that of imposed by the space discretisation.

	$h = \frac{1}{2}$	$h = \frac{1}{4}$	$h = \frac{1}{8}$	$h = \frac{1}{16}$
$p = 1$	—	-7.9554e-06	-4.0558e-07	-2.3730e-08
$p = 2$	-1.6866e-05	-7.8671e-07	-4.8152e-08	—
$p = 3$	-3.2488e-06	-2.0035e-07	-1.2516e-08	—

Table XV: Imaginary part of the numerical frequency, $\mathrm{Im}(\omega_h^\tau)$, for the LEX4 time-integration method, where the semi-discrete numerical frequencies ω_h are taken from Table X. This term is responsible for numerical dissipation.

	$h = \frac{1}{2}$	$h = \frac{1}{4}$	$h = \frac{1}{8}$	$h = \frac{1}{16}$
$p = 1$	—	-6.9642e-07	-1.6998e-08	-4.9043e-10
$p = 2$	-1.7825e-06	-3.9053e-08	-1.1891e-09	—
$p = 3$	-2.3027e-07	-7.0689e-09	-2.2071e-10	—

Table XVI: Imaginary part of the numerical frequency, $\mathrm{Im}(\omega_h^\tau)$, for the SSPRK(4, 3) time-integration method, where the semi-discrete numerical frequencies ω_h are taken from Table X. This term is responsible for numerical dissipation.

	$h = \frac{1}{2}$	$h = \frac{1}{4}$	$h = \frac{1}{8}$	$h = \frac{1}{16}$
$p = 1$	—	-7.5911e-04	-8.0688e-05	-9.5692e-06
$p = 2$	-1.3346e-03	-1.3217e-04	-1.6251e-05	—
$p = 3$	-3.8256e-04	-4.7337e-05	-5.9156e-06	—

6. Concluding remarks

We have investigated the time-dependent second-order Maxwell equation in three spatial dimensions. A direct comparison between the high-order DG-FEM and the high-order $H(\mathrm{curl})$-conforming FEM on both structured and unstructured meshes was provided when $H(\mathrm{curl})$-conforming hierarchic basis functions are used. It has revealed that, in case hierarchic basis functions are used, the computational cost is already lower for DG-FEM when $p = 3$, or even $p = 2$ on unstructured meshes. The computational tests have highlighted the fact that the inclusion of moderate conductivity renders many of the popular time-integration methods uncompetitive owing to a stringent time-step restriction. In these cases, global or local Richardson extrapolations based on the second-order composition method provide a viable alternative as they treat the conductivity term implicitly.

Through a numerical dispersion and dissipation analysis, we have also shown that the spatial discretisation dominates the frequency error as long as the order of the time integration is at least the same as the order of the spatial discretisation. Since the semi-discrete system is symmetric and therefore conserves (the discrete) energy, applying a composition method to integrate in time results in a fully-discrete scheme that also conserves (the discrete) energy.

Acknowledgments

This research was supported by the Dutch government through the national program BSIK: knowledge and research capacity, in the ICT project BRICKS (`http://www.bsik-bricks.nl`), theme MSV1.

[1] J.-C. Nédélec, Mixed finite elements in $\mathbf{R}^3$, Numer. Math. 35 (3) (1980) 315–341.

[2] J.-C. Nédélec, A new family of mixed finite elements in $\mathbf{R}^3$, Numer. Math. 50 (1) (1986) 57–81.

[3] A. Bossavit, A rationale for 'edge-elements' in 3-D fields computations, IEEE Trans. Magn. 24 (1) (1988) 74–79.

[4] A. Bossavit, Solving Maxwell equations in a closed cavity, and the question of 'spurious modes', IEEE Trans. Magn. 26 (2) (1990) 702–705.

[5] B. Cockburn, C.-W. Shu, Runge-Kutta discontinuous Galerkin methods for convection-dominated problems, J. Sci. Comput. 16 (3) (2001) 173–261.

[6] J. S. Hesthaven, T. Warburton, Nodal high-order methods on unstructured grids. I. Time-domain solution of Maxwell's equations, J. Comput. Phys. 181 (1) (2002) 186–221.

[7] J. S. Hesthaven, T. Warburton, Nodal discontinuous Galerkin methods, Vol. 54 of Texts in Applied Mathematics, Springer, New York, 2008, algorithms, analysis, and applications.

[8] M. Ainsworth, J. Coyle, Hierarchic finite element bases on unstructured tetrahedral meshes, Internat. J. Numer. Methods Engrg. 58 (14) (2003) 2103–2130.

[9] P. Šolín, K. Segeth, I. Doležel, Higher-order finite element methods, Studies in Advanced Mathematics, Chapman & Hall/CRC, Boca Raton, FL, 2004.

[10] L. Demkowicz, J. Kurtz, D. Pardo, M. Paszyński, W. Rachowicz, A. Zdunek, Computing with *hp*-adaptive finite elements. Vol. 2, Chapman & Hall/CRC Applied Mathematics and Nonlinear Science Series, Chapman & Hall/CRC, Boca Raton, FL, 2008, frontiers: three dimensional elliptic and Maxwell problems with applications.

[11] R. Hiptmair, Finite elements in computational electromagnetism, Acta Numer. 11 (2002) 237–339.

[12] P. Monk, Finite element methods for Maxwell's equations, Numerical Mathematics and Scientific Computation, Oxford University Press, New York, 2003.

[13] M. J. Grote, A. Schneebeli, D. Schötzau, Interior penalty discontinuous Galerkin method for Maxwell's equations: energy norm error estimates, J. Comput. Appl. Math. 204 (2) (2007) 375–386.

[14] M. J. Grote, A. Schneebeli, D. Schötzau, Interior penalty discontinuous Galerkin method for Maxwell's equations: optimal L^2-norm error estimates, IMA J. Numer. Anal. 28 (3) (2008) 440–468.

[15] M. J. Grote, D. Schötzau, Optimal error estimates for the fully discrete interior penalty DG method for the wave equation, J. Sci. Comput. 40 (1-3) (2009) 257–272.

[16] J. Diaz, M. J. Grote, Energy conserving explicit local time stepping for second-order wave equations, SIAM Journal on Scientific Computing 31 (3) (2009) 1985–2014. doi:10.1137/070709414.
URL http://link.aip.org/link/?SCE/31/1985/1

[17] M. A. Botchev, J. G. Verwer, Numerical integration of damped Maxwell equations, SIAM J. Sci. Comput. 31 (2) (2009) 1322–1346. doi:10.1137/08072108X.
URL http://link.aip.org/link/?SCE/31/1322/1

[18] R. Rieben, D. White, G. Rodrigue, High-order symplectic integration methods for finite element solutions to time dependent Maxwell equations, IEEE Trans. Antennas and Propagation 52 (8) (2004) 2190–2195.

[19] S. Benhassine, J. Carpes, L. Pichon, Comparison of mass lumping techniques for solving the 3D Maxwell's equations in the time domain, IEEE Trans. Magn. 36 (4) (2000) 1548–1552.

[20] A. Fisher, R. N. Rieben, G. H. Rodrigue, D. A. White, A generalized mass lumping technique for vector finite-element solutions of the time-dependent Maxwell equations, IEEE Trans. Antennas and Propagation 53 (9) (2005) 2900–2910.

[21] Z. Ye, L. Du, Z. Fan, R. Chen, Mass lumping techniques combined with 3D time-domain finite-element method for the vector wave equation, in: International Conference on Microwave and Millimeter Wave Technology, 2008, Vol. 3, 2008, pp. 1307–1310.

[22] B. He, F. L. Teixeira, Differential forms, Galerkin duality, and sparse inverse approximations in finite element solutions of Maxwell equations, IEEE Trans. Antennas and Propagation 55 (5) (2007) 1359–1368.

[23] J. Jin, The finite element method in electromagnetics, 2nd Edition, Wiley-Interscience [John Wiley & Sons], New York, 2002.

[24] D. N. Arnold, F. Brezzi, B. Cockburn, L. D. Marini, Unified analysis of discontinuous Galerkin methods for elliptic problems, SIAM J. Numer. Anal. 39 (5) (2001/02) 1749–1779.

[25] D. Sármány, F. Izsák, J. J. W. van der Vegt, High-order accurate discontinuous Galerkin method for the indefinite time-harmonic Maxwell equations, Memorandum 1889, Department of Applied Mathematics, University of Twente, Enschede, the Netherlands, available at http://eprints.eemcs.utwente.nl/14852/01/memo1889.pdf (January 2009).

[26] F. Brezzi, G. Manzini, D. Marini, P. Pietra, A. Russo, Discontinuous finite elements for diffusion problems, in: Atti Convegno in onore di F. Brioschi (Milan, 1997), Istitutto Lombardo, Accademia di Scienza e Lettere, Milan, Italy, 1999, pp. 197–217.

[27] F. Bassi, S. Rebay, G. Mariotti, S. Pedinotti, M. Savini, A high order accurate discontinuous finite element method for inviscid and viscous turbomachinery flows, in: Proceedings of the 1997 2nd European Conference on Turbomachinery - Fluid Dynamics and Thermodynamics, (Antwerpen, Belgium), 1997, pp. 99–108.

[28] R. J. Spiteri, S. J. Ruuth, A new class of optimal high-order strong-stability-preserving time discretization methods, SIAM J. Numer. Anal. 40 (2) (2002) 469–491.

[29] S. J. Ruuth, Global optimization of explicit strong-stability-preserving Runge-Kutta methods, Math. Comp. 75 (253) (2006) 183–207.

[30] S. Gottlieb, S. J. Ruuth, Optimal strong-stability-preserving time-stepping schemes with fast downwind spatial discretizations, J. Sci. Comput. 27 (1-3) (2006) 289–303.

[31] E. Hairer, C. Lubich, G. Wanner, Geometric numerical integration, Vol. 31 of Springer Series in Computational Mathematics, Springer-Verlag, Berlin, 2002, structure-preserving algorithms for ordinary differential equations.

[32] R. I. McLachlan, On the numerical integration of ordinary differential equations by symmetric composition methods, SIAM J. Sci. Comput. 16 (1) (1995) 151–168.

[33] J. M. Sanz-Serna, M. P. Calvo, Numerical Hamiltonian problems, Vol. 7 of Applied Mathematics and Mathematical Computation, Chapman & Hall, London, 1994.

[34] G. Rodrigue, D. White, A vector finite element time-domain method for solving Maxwell's equations on unstructured hexahedral grids, SIAM J. Sci. Comput. 23 (3) (2001) 683–706.

[35] P. Houston, I. Perugia, A. Schneebeli, D. Schötzau, Interior penalty method for the indefinite time-harmonic Maxwell equations, Numer. Math. 100 (3) (2005) 485–518.

[36] L. Pesch, A. Bell, H. Sollie, V. R. Ambati, O. Bokhove, J. J. W. Van Der Vegt, hpGEM—a software framework for discontinuous Galerkin finite element methods, ACM Trans. Math. Software 33 (4) (2007) Art. 23, 25.

[37] S. Balay, K. Buschelman, W. D. Gropp, D. Kaushik, M. G. Knepley, L. C. McInnes, B. F. Smith, H. Zhang, PETSc Web page, http://www.mcs.anl.gov/petsc (2001).

[38] G. L. G. Sleijpen, H. A. van der Vorst, A Jacobi-Davidson iteration method for linear eigenvalue problems, SIAM J. Matrix Anal. Appl. 17 (2) (1996) 401–425.

[39] G. L. G. Sleijpen, H. A. van der Vorst, A Jacobi-Davidson iteration method for linear eigenvalue problems, SIAM Rev. 42 (2) (2000) 267–293.